VICTORIA UNIVERSITY
MELBOURNE AUSTRALIA

Age-related anatomical variations and the impact of adenoid hypertrophy on nasal airflow in Asian children

Age-related anatomical variations and the impact of adenoid hypertrophy on nasal airflow in Asian children

Zhenzhen Hu [a,b], Junming Chen [c], Ya Zhang [b,*], Ying Wang [a], Yulin Zhao [a], Guoxi Zheng [b], Shaokoon Cheng [d], Kiao Inthavong [c], Jingliang Dong [c,e,f,**]

[a] Department of Rhinology, The First Affiliated Hospital of Zhengzhou University, Zhengzhou 450052, China
[b] Department of Otolaryngology Head and Neck Surgery, The Second Affiliated Hospital of Xi'an Jiaotong University, Xi'an, Shaanxi 710004, China
[c] Mechanical, Manufacturing and Mechatronic Engineering, School of Engineering, RMIT University, Bundoora 3083, Australia
[d] School of Engineering, Faculty of Science and Engineering, Macquarie University, Australia
[e] Institute for Sustainable Industries & Liveable Cities, Victoria University, PO Box 14428, Melbourne, VIC 8001, Australia
[f] First Year College, Victoria University, Footscray Park Campus, Footscray, VIC 3011, Australia

ARTICLE INFO

ABSTRACT

The human nasal airway grows rapidly in childhood and some children develop pathological changes of adenoid hypertrophy (AH), leading to substantial alterations in airflow dynamics. To ensure the healthy growth of children, we quantified the growth of the nasal airway and analyzed the nasal airflow field and nasal function. Models of 26 children aged 3–12 years were constructed, and the geometric dimensions of the nasal airway were quantified based on parameters such as surface area, volume, cross-sectional area, and hydraulic diameter. Computational fluid dynamics (CFD) methods were employed to simulate the nasal airflow field. Virtual adenoidectomy was performed on children with severe AH, and partitioned airflow volume and warming and humidification were quantitatively compared before and after surgery. The results showed that the turbinate area in children aged 3–12 develops most rapidly and constitutes the main form of the complex shape of the nasal cavity. The majority of airflow in children's nasal cavities passes through the main nasal passage and the middle meatus, with a small portion of the airflow passing though the olfactory fissure. After adenoidectomy, more airflow is redirected to the olfactory region, and the imbalance in airflow distribution between the left and right nasal cavities is reduced. Virtual post-operatively, the warming and humidification of the nasal cavity, especially in the nasopharynx, has decreased, which is significantly correlated with the surface area-to-volume ratio of the airway. The findings contribute to a better understanding of the growth and development of nasal airways in Asian children.

1. Introduction

The upper respiratory tract consists nasal cavity and nasopharynx and is the channel responsible for connecting the lungs and the external environment [1,2]. The immature defense mechanisms of the respiratory tract make children more susceptible to respiratory disease compared to adults [3], which is also a major cause of pediatric morbidity in the United States and other developed countries. As the first defense of the respiratory system, the nasal cavity has a warming, humidification and filtering effect on inhaled air [4], which helps to prevent potential damage to the fragile lungs. Previous studies have

shown that altered nasal airway anatomy and associated nasal airflow patterns are the primary determinants of impaired nasal function [5,6]. Nasal surgery inevitably results in alterations of the intranasal structures, thereby impacting nasal physiological function [7–9]. Therefore, by understanding the changes in upper airway morphology and associated airflow patterns during childhood development, we can treat impaired physiological function in pediatric patients more effectively.

Statistics show that 34.46 % of children and adolescents develop adenoid hypertrophy (AH) as they grow [10], with adenoids usually reaching their maximum size at 6–7 years of age and then regressing during puberty [11]. AH is one of the most common causes of upper

---

airway obstruction and obstructive sleep apnea (OSA) in children [12]. The common clinical symptoms are nasal congestion, running nose, snoring, mouth breathing, loss of appetite and stunting, and adenoidal facies in some children. The most common clinical intervention for children who fail to respond to medications is adenoidectomy [13]. The resulting structural alteration of the nasal cavity may further affect the pediatric nasal function. In order to promote an optimal recovery and enhance the life quality of post-operative children, it is necessary to explore the changes in nasal warming and humidification function in children before and after adenoidectomy.

To date, most studies on upper airway flow characteristics and nasal function have focused on adult subjects [14–16], while research involving pediatric subjects remains relatively limited. Xi et al. [17] reported the structure of the upper airway and the associated aerodynamic presentation in a 5-year-old child. Subsequently, Xi et al. [18] studied the growth of the naso-laryngeal airway in children aged 10 days, 7 months, 3 years and 5 years. The results showed that there were significant differences in the morphology and geometric dimensions of the nasal airways of the four subjects, with the turbinate region in particular experiencing the most significant growth during the first 5 years of life. Dong et al. [19] numerically simulated the airflow fields of nasal cavity models of 5, 24 and 77 years old. Due to significant anatomical variations among the nasal cavities, the airflow distributions differed markedly, particularly in terms of localised ventilation into the olfactory region. Recently, Sun et al. [20] studied the deposition of ultrafine particles in the nasal airways of children, adults, and the elderly, and found that the elderly and children exhibited unique patterns that differed from those of adults. Zhou et al. [21] found that the longer length and more complex geometry of the adult nasal replicas in the anterior turbinate region could be responsible for the higher particle deposition rate in this region compared to children. There were several growth spurts in different parts of the nasal cavity with age, which is consistent with the results of the anatomy experiment by Samolinski et al. [22]. Our previous work investigated the effects of different degrees of AH on pediatric upper airway aerodynamics, and showed that for the upper airway with adenoidal-nasopharyngeal (AN) ratio greater than 0.7, the nasopharynx had a significant flow-limiting effect [23]. Exploration of the nasal warming and humidification function in children has been scarcely described previously, and it remains unclear. An exception is the study by Moreddu et al. [24], who analyzed the physiological nasal airflow and thermal distribution in a neonate aged 0–28 days by computational fluid dynamics (CFD) techniques. The results showed that the nasal valve area is crucial for air warming in neonates, with about 70 % of air warming conducted in this area. If necessary, surgical intervention should respect the anatomy of this area to restore normal airflow and warming. Additionally, in adult studies, Keck et al. [25,26] observed rapid air warming in the nasal valve areas using in vivo captors. Subsequently, computational fluid dynamics studies by Sommer et al. [27] and Hanida et al. [28] confirmed this finding. The temperature difference between air and mucosa is the determinant for water transfer from the mucosal surface to inhaled air [26,29]. Due to the increase in temperature, moisture transport becomes more efficient and vice versa. Dayal et al. [30] indicated that total inferior turbinectomy or total medial turbinectomy increases nasal airflow and also impairs nasal air modulation, and extra caution should be taken with regard to these post-operative complications.

Although extensive research has been conducted, previous studies have primarily focused on analyzing a limited number of individual models in adults, leading to findings that are not representative of the broader population. Due to the rapid growth in children, growth spurt in nasal cavity, age and even ethnicity can lead to differences in geometry and internal flow fields [31,32], and combining multiple models across wide age ranges can reduce some level of error and lead to a relatively common conclusion.

In response to the above-mentioned need, this study established anatomically precise upper airway models of 26 Asian children aged

Table 1
Demographic information of research subjects.

Subject	Age	Sex	History of nasal surgery	AN ratio	Adenoid hypertrophy
Subject 1	3Y	F	None	0.72	Moderate
Subject 2	3Y	M	None	0.91	Severe
Subject 3	3Y	M	None	0.80	Severe
Subject 4	4Y	F	None	0.86	Severe
Subject 5	4Y	M	None	0.87	Severe
Subject 6	4Y	M	None	0.90	Severe
Subject 7	5Y	M	None	0.75	Moderate
Subject 8	5Y	F	None	0.88	Severe
Subject 9	5Y	M	None	0.73	Moderate
Subject 10	6Y	F	None	0.76	Moderate
Subject 11	6Y	F	None	0.86	Severe
Subject 12	6Y	M	None	0.65	Mild
Subject 13	7Y	M	None	0.77	Moderate
Subject 14	7Y	M	None	0.61	Mild
Subject 15	8Y	M	None	0.82	Severe
Subject 16	8Y	F	None	0.86	Severe
Subject 17	9Y	M	None	0.47	No
Subject 18	9Y	M	None	0.54	No
Subject 19	10Y	M	None	0.41	No
Subject 20	10Y	F	None	0.58	No
Subject 21	10Y	F	None	0.61	Mild
Subject 22	11Y	M	None	0.45	No
Subject 23	11Y	F	None	0.65	Mild
Subject 24	11Y	M	None	0.71	Moderate
Subject 25	11Y	M	None	0.50	No
Subject 26	12Y	M	None	0.40	No

3–12 years, quantified the geometric dimensions of the nasal airway, conducted numerical simulations of nasal airflow dynamics, and analyzed the partitioned airflow in the nasal cavity. To further investigate the partitioned airflow and functional changes in the nasal cavities of children with AH, we performed virtual adenoidectomy on the four most severe AH cases and quantitatively compared the zonal airflow volume and warming and humidification function of the nasal cavity before and after surgery. This study addressed the gaps in existing research for Asian nasal cavities in this age group. The findings of this study contribute to a better understanding of the growth and development of the upper airway in children and can provide guidance for adenoidectomy treatment to better protect the function of the nasal cavity in children.

2. Materials and methods

This section describes the methodology for constructing pediatric upper airway models, conducting numerical simulations, and performing post-processing analyses.

2.1. Data collection

A total of 26 Asian children aged 3–12 years were recruited as volunteers for this study, including both healthy subjects and children with
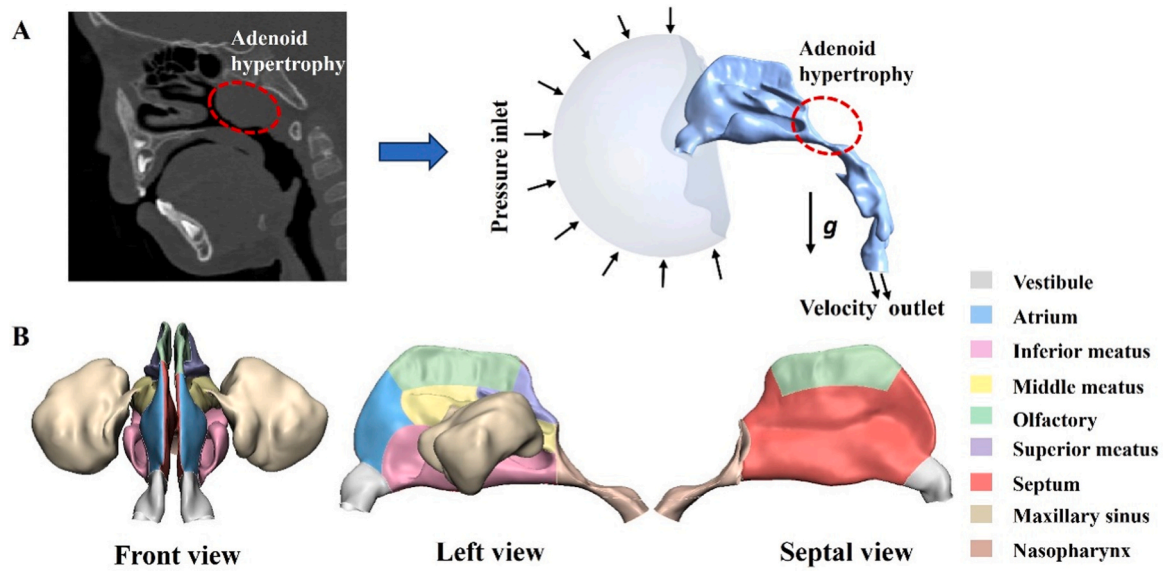
Fig. 1. Boundary condition settings and anatomical partition of the nasal cavity model (using Subject 2 as an example). (A) Boundary condition settings for the nasal cavity. (B) Anatomical partition of the nasal cavity. Due to space constraints, all figures use the same model for demonstration.
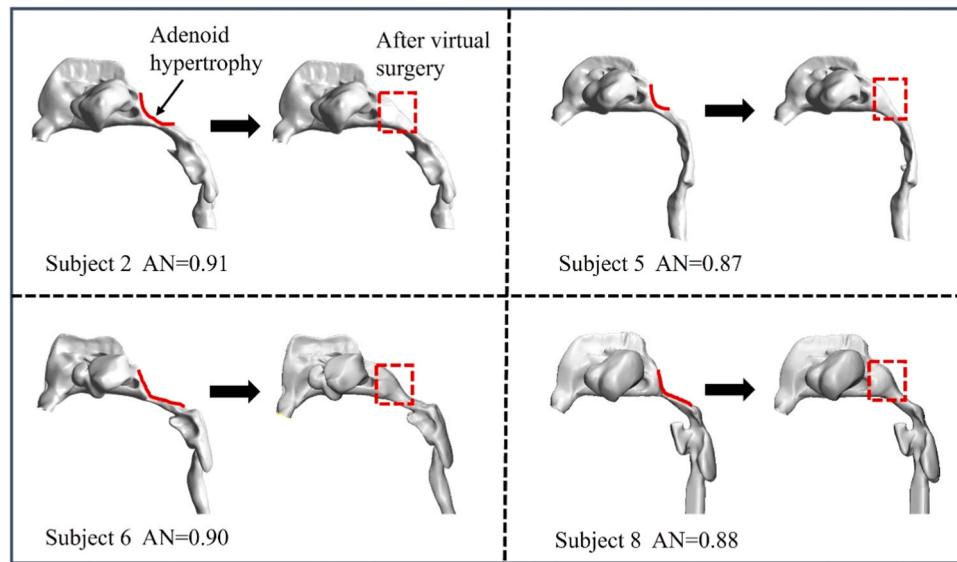

Fig. 2. Pediatric nasal airway models before and after virtual adenoidectomy.

AH. All children underwent computerized tomography (CT) scans with a slice thickness of 0.5 mm, covering the entire upper airway. The detailed information for each child is presented in Table 1. This study was reviewed and approved by the Ethics Committee of the Second Affiliated Hospital of Xi'an Jiaotong University (2022–186). The guardians of all participants were informed about the use of CT, and their consent was obtained. Based on the CT scan images, it was observed that the majority of children had AH, with varying degrees of narrowness in the nasopharynx. The A/N ratio, defined as the ratio of adenoid thickness to nasopharyngeal width, reflects the size of the adenoids and the patency of the nasopharyngeal airway [33]. When the AN ratio is greater than 0.6, it is considered as AH [34]. The degree of adenoid obstruction of the nasopharyngeal airway can be classified based on the AN ratio as mild (0.60–0.69), moderate (0.70–0.79), and severe (0.80–0.89) [35]. The AN ratio was measured for all children, and the results are shown in Table 1. The detailed AN ratio measurement method can be found in our previous work [23,36], where the correlation between the AN ratio, adenoid tissue, and flow resistance has been extensively discussed.

2.2. Airway reconstruction

CT images in Digital Imaging and Communications in Medicine (DICOM) format were imported into 3D Slicer (https://www.slicer.org/), and a radiodensity threshold of −1024 to −350 Hounsfield Units (HU) was used to distinguish air-filled spaces from soft tissues, in order to reconstruct a three-dimensional model of the upper airway including facial features (Fig. 1A). The reconstructed geometric model was imported in STL format into ANSYS SpaceClaim (ANSYS Inc., Canonsburg, Pennsylvania) for surface smoothing and regional segmentation. Based on anatomical and functional characteristics of the nasal cavity, all models were divided into nine regions (Fig. 1B). For children with AH, we selected four subjects with the most severe cases, Subject 2 (AN ratio = 0.91), Subject 5 (AN ratio = 0.87), Subject 6 (AN ratio = 0.90), and Subject 8 (AN ratio = 0.88), to undergo virtual adenoidectomy (Fig. 2), in order to conduct a comparative study of airflow dynamics and air-conditioning (warming and humidification) functions before and after surgery. The nasopharyngeal region of the upper airway
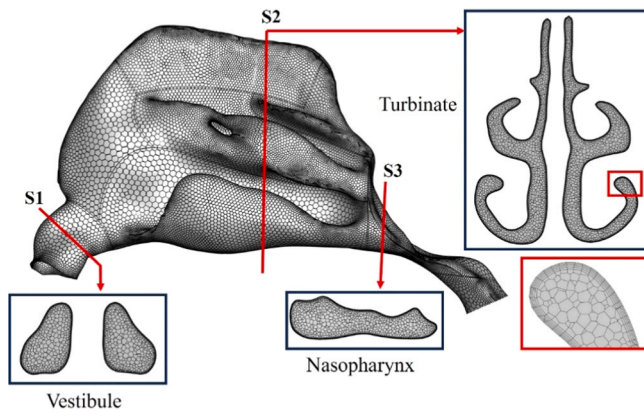
Fig. 3. Hybrid prism-polyhedral mesh of the nasal cavity wall and internal cross-sections. S1: Nasal vestibule, S2: Turbinate, S3: Nasopharynx.

model was modified in 3D Slicer to remove the hypertrophic adenoid tissue and restore the nasopharyngeal airway to a normal anatomical state, resulting in a virtual post-operative model. The virtual surgery was performed under the guidance of an attending physician with professional clinical expertise. Apart from the modifications in the obstructed nasopharyngeal region, the remaining structures of the virtual post-operative model were identical to those of the original model.

ICEM CFD and Fluent meshing 2021 R1 (ANSYS Inc., Canonsburg, Pennsylvania) software are used for meshing. All model in this study uses a high-quality hexahedral mesh with five prism layers near the wall surface, a first layer with an aspect ratio of 8 and a growth rate of 1.2 (Fig. 3). Compared with traditional tetrahedral meshes, hexahedral meshes exhibit lower sensitivity to stretching, better numerical convergence, and improved computational efficiency [37]. Mesh independence tests were conducted using four mesh configurations: coarse (element size 5.0 mm), medium (1.0 mm), fine (0.5 mm), and ultra-fine (0.1 mm) (Fig. 4A). A representative line was drawn across the nasopharyngeal cross-section, and velocity values along this line were extracted from each mesh configuration for comparison (Fig. 4B). When the number of mesh elements exceeded 2.6 million (element size 0.5 mm), corresponding to approximately 9.1 million tetrahedral elements, the differences in velocity magnitude were negligible, indicating high simulation consistency and sufficient computational accuracy to accurately capture the relevant flow field characteristics. To balance computational efficiency and simulation accuracy, a fine mesh

configuration (element size of 0.5 mm) was used for generating the meshes of all nasal airway models in this study.

In our previous work, experimental measurements were performed to validate the accuracy of the CFD models [23]. A 1:1 scale solid model of the pediatric upper airway was fabricated using stereolithography (STL) 3D printing technology. In vitro Rhinomanometry was conducted (Equipment Model NR6, GM Instruments) on children's nasal solid model, and good agreement was achieved between the measurements and numerical predictions across a wide range of inhalation and exhalation flow rates. Since the modeling method is consistent, the accuracy of the pediatric model simulations in this study can be used for further data analysis.

2.3. CFD simulation and boundary conditions

The governing equation of this study is incompressible viscous fluid Navier-Stokes equations, Ansys Fluent 2021 R1 (ANSYS, Inc., Canonsburg, Pennsylvania) were used to conduct the simulation. The low-Reynolds-number k-ω SST model is suitable for laminar-transitional-turbulent flow conditions and can accurately predict velocity profiles, pressure drops, and shear stresses in complex flow regimes [17,18]. Given the irregular internal structures of the pediatric upper airway, this study employed the low-Reynolds-number k-ω SST turbulence model to simulate airflow dynamics, and the SIMPLE algorithm was used for pressure-velocity coupling. To verify the convergence of the simulation result, the residual value was set to 10^{-9}. All models used in this study either reached the predetermined residual values, or the residual lines showing converged to stable values and physical quantities such as pressure and velocity reached a stable value and met convergence conditions.

Fig. 1A depicts the boundary condition setup for all nasal airway models, which has been utilized in our previous studies [38,39]. Specifically, a hemispherical zone was created in front of the face, with the hemispherical surface designated as the pressure inlet, while the downstream nasopharynx opening was set as the velocity outlet. Hofmann [40] proposed analytical expressions that describe the age-dependent variation of respiratory parameters during postnatal human lung development, including the calculation of tidal volume and respiratory frequency:

$$TV(t) = 21.7 + 35.13t - 0.64t^2 \# \tag{1}$$

where TV (ml/breath) is the volume of air inhaled or exhaled per breath, and t (years) represents age.
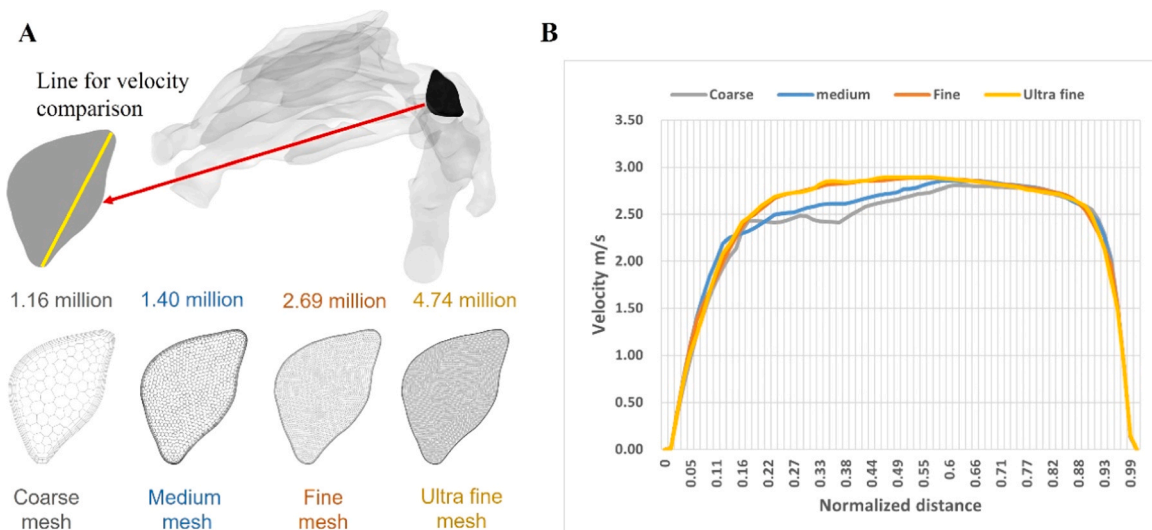

Fig. 4. (A) Location of the nasopharyngeal line. (B) Mesh independence test.

Table 2
Volumatic flow rate calculations based on empirical correlation proposed by Hofmann (1982).

Age	Respiratory rate (breaths/min)	Tidal volume (ml/breath)	Flow rate (L/min)
3	24	121	7.84
4	22	152	9.03
5	20	181	9.77
6	19	209	10.72
7	18	236	11.47
8	18	262	12.73
9	17	286	13.13
10	17	309	14.18
11	16	331	14.30
12	16	351	15.16

$$RF(t) = \frac{15.17}{0.25t + 0.5} + 11.75 \# \tag{2}$$

where RF (breaths/min) denotes the number of breaths completed per minute, and t (years) represents age.

The calculated values for tidal volume, respiratory frequency, and respiratory flow rate in children aged 3–12 years are shown in Table 2.

The primary function of the nasal cavity is to warm and humidify inhaled air before it enters the lower respiratory tract, a process that can be disrupted by local diseases or surgical interventions. Currently, changes in children's nasal warming and humidifying function before and after adenoidectomy remain largely unknown, limiting objective guidance for clinical treatment. Conducting in vivo measurements in children's nasal cavities is challenging due to ethical considerations and the physical constraints of the narrow space. Numerical simulation presents a promising alternative for studying nasal function. Moreddu et al. [24] conducted a simulation of the neonatal nasal cavity, using standard temperature values from the literature. Sommer et al. [27] and Lindemann et al. [41] inserted small sensors and miniature
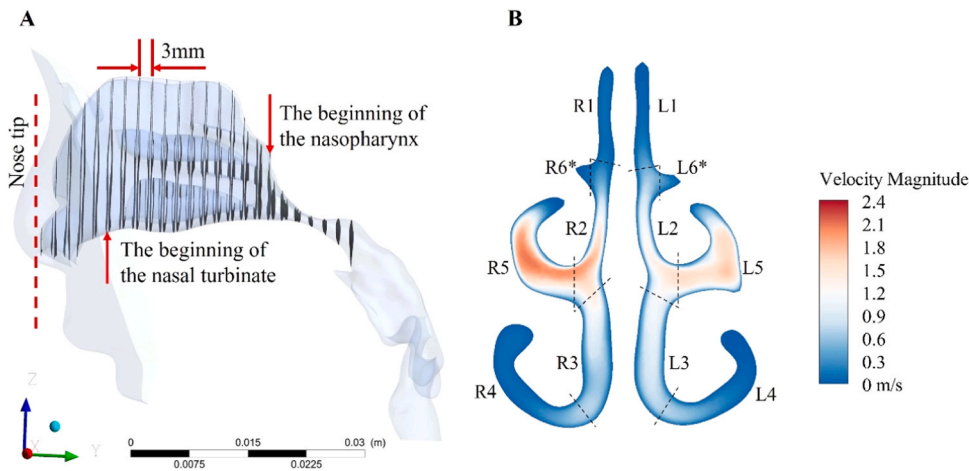
Fig. 5. (A) Schematic of cross-sectional slice of nasal model. (B) Schematic diagram region division of central cross-section plane in nasal cavities. L1/R1: Olfactory region, L2/R2: Middle of the main nasal passage, L3/R3: Lower part of the main nasal passage, L4/R4: Inferior meatus, L5/R5: Middle meatus, L6/R6: Superior meatus (*some models superior meatus not visible at central plane).

Fig. 6. Slices taken along left nasal cavity and nasopharynx in the original and virtual post-operative models.

Table 3
Surface areas of the nasal regions.

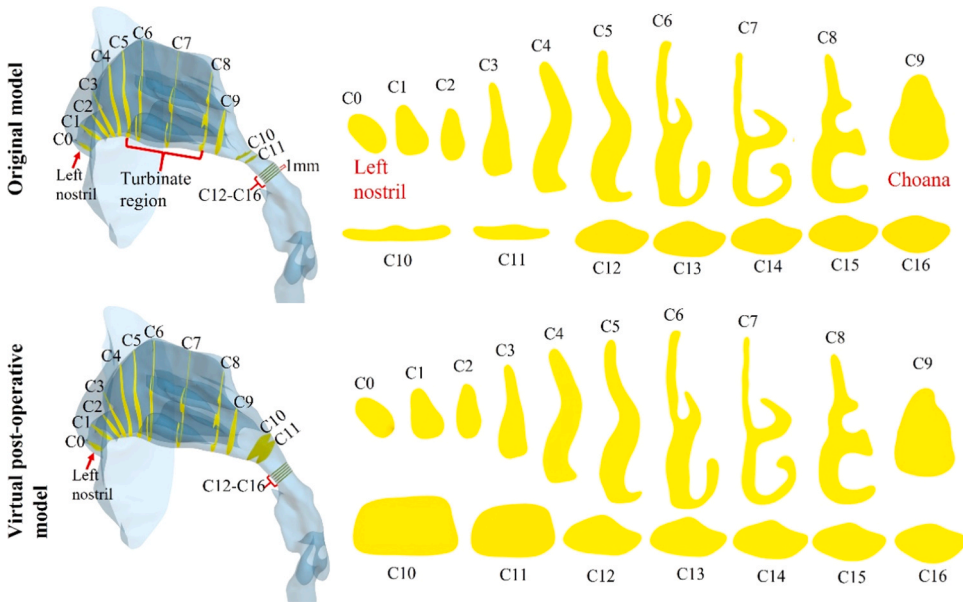| Region	Airway Surface Area (cm^2)									
	3Y	4Y	5Y	6Y	7Y	8Y	9Y	10Y	11Y	12Y
Vestibule and valve	2.66	3.06	3.06	2.81	3.62	3.23	3.59	3.74	4.44	3.68
Atrium	2.07	2.18	2.21	2.09	2.86	2.43	2.73	2.60	2.92	3.04
Septum	11.90	12.04	13.13	13.47	16.05	15.39	16.96	17.11	18.66	16.91
Turbinate region	22.86	24.45	26.03	25.85	31.57	34.63	31.75	35.83	40.20	35.12
Olfactory	4.54	4.37	5.05	4.84	5.29	5.58	5.43	6.34	7.18	5.99
Nasopharynx	10.50	10.88	12.69	12.78	13.07	15.12	18.30	18.34	16.14	12.28
Left nostril	0.41	0.42	0.50	0.41	0.55	0.42	0.51	0.65	0.63	0.53
Right nostril	0.40	0.43	0.51	0.41	0.59	0.42	0.52	0.69	0.68	0.54
LC	44.25	46.18	48.94	49.49	58.76	61.29	59.88	65.86	71.87	65.44
RC	43.81	46.00	50.04	48.63	60.03	61.19	61.03	65.36	74.94	64.01
Total (LC&RC)	88.06	92.18	98.98	98.11	118.79	122.48	120.9	131.21	146.81	129.45

RC: right cavity, LC: left cavity.

thermocouples into the human nasal cavity to measure temperature and humidity for numerical simulations, respectively.

The Energy Equation and Species Transport models were enabled in Fluent to perform numerical simulations of heat and moisture transfer. The detailed boundary conditions for this study are set as follows [24,27, 41]: The airway wall was assumed as rigid and non-slip (zero velocity). The hemisphere in front of the face was designated as the "pressure inlet" (pressure set to 0 Pa), with a temperature of 20°C (293 K) and a relative humidity of 30 % (absolute humidity of 5.18 mg/L). The temperature of the nasal wall was set at 34°C (307 K) with a relative humidity of 100 %, corresponding to an absolute humidity of 37.5 mg/L. The outlet of the calculation domain was assigned as a "velocity outlet," with the velocity calculated by dividing the volumetric inhalation flow rate with the outlet area, and a temperature set to 30°C (303 K).

Post-processing was performed using CFD-Post and Tecplot. To analyze the influence of age on airway morphology, vertical cross-sections with evenly spaced intervals (3 mm) were created from the anterior nostril to the nasopharynx across 26 nasal models (Fig. 5 A). This setup allowed for comparison of cross-sectional areas and hydraulic diameters across ages. Additionally, to enable a detailed analysis of the airflow within the nasal cavity, the central cross-sectional plane, positioned anterior to the superior turbinate, was divided into multiple regions based on the nasal meatus structure [42]. The detailed regional partitions are illustrated in Fig. 5B. Due to the narrow opening of the maxillary sinus, airflow from the main nasal passage into the maxillary sinus is limited and constitutes only a small portion of the total airflow. Consequently, only airflow passing through the main nasal passage was analyzed.

To compare the nasal warming and humidification functions between the original and virtual post-operative models, 12 cross-sections perpendicular to the primary airflow direction were established at key anatomical locations within the upper airway to generate temperature and humidity contour maps (Fig. 6). Using the left nasal cavity as a reference, the anterior nostril was designated as C0. Cross-sections C1 to C3 were positioned within the nasal vestibule and nasal valve. Cross-

sections C4 to C8 were located sequentially in the nasal expansion area, at the head of the inferior turbinate, the head of the middle turbinate, the middle portion of the inferior turbinate, and the posterior portion of the inferior turbinate. Finally, cross-sections C9 to C11 were positioned at the choana and within the nasopharynx. In addition, five extra slices (C12–C16) were created downstream of the nasopharynx at uniform intervals of 1 mm to facilitate data comparison between the original and virtual post-operative airways in assessing nasal air-conditioning function.

2.4. Statistical analyses

A *t*-test was employed to compare the temperature and humidity in the pharynx before and after virtual surgery. Spearman correlation analysis was conducted to examine factors influencing pharyngeal temperature and humidity. A significance level of $p < 0.05$ was considered statistically significant. Statistical analysis was performed using SPSS 21.0 software (SPSS Inc., Chicago, Illinois).

3. Results and discussion

This section describes the geometric characteristics of the nasal airways in children aged 3–12 years, their airflow dynamics, and the regional airflow volumes, and further analyzes the effects of virtual surgery on regional airflow distribution and nasal air conditioning (warming and humidifying) function.

3.1. Anatomical features of the nasal airways

Tables 3 and 4 summarize the surface area and volume of the nasal airway in children aged 3–12 years. To provide representative insights across age groups, the geometric dimensions are presented as the mean values for each age group, enhancing the conciseness and interpretability of the results. Geometric analysis shows that younger children have smaller nostrils, less developed nasal turbinate structures, and a

Table 4
Volumes of the nasal regions.

| Region	Airway Volume (cm^3)									
	3Y	4Y	5Y	6Y	7Y	8Y	9Y	10Y	11Y	12Y
Vestibule and valve	0.41	0.49	0.49	0.43	0.63	0.55	0.68	0.68	0.86	0.69
Atrium	0.42	0.48	0.44	0.42	0.67	0.51	0.63	0.56	0.73	0.84
Turbinate region	3.9	3.61	3.96	3.93	5.44	4.34	4.77	6.43	7.94	9.32
Olfactory	0.31	0.3	0.39	0.31	0.42	0.26	0.3	0.42	0.65	0.47
Nasopharynx	1.87	1.93	2.76	2.85	3.36	2.84	6.38	6.15	4.79	3.78
LC	4.98	4.93	5.53	5.15	6.51	6.00	6.3	7.25	9.07	11.16
RC	5.11	4.81	5.02	5.04	7.81	5.31	6.47	8.94	11.3	11.45
Total (LC&RC)	10.10	9.75	10.55	10.19	14.32	11.31	12.77	16.19	20.37	22.61

RC: right cavity, LC: left cavity.
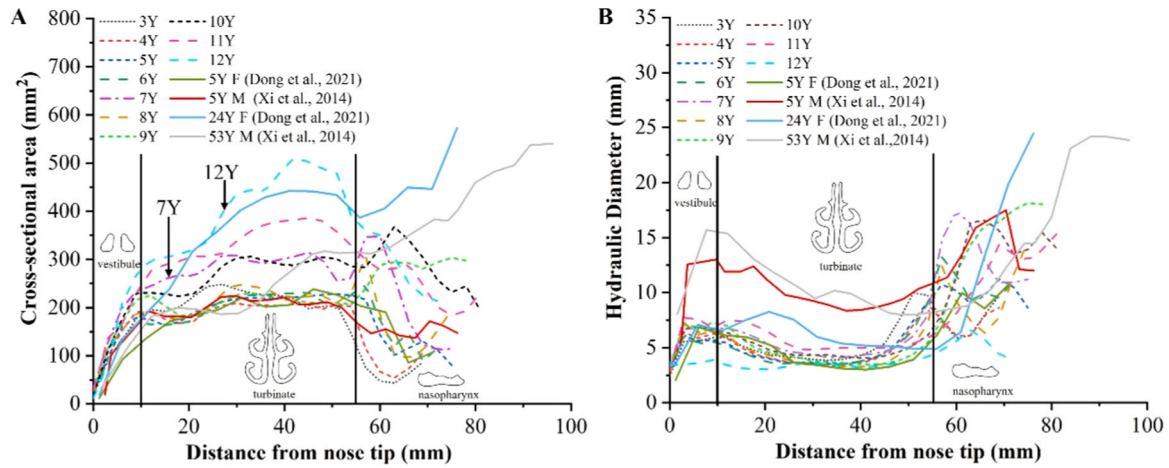
Fig. 7. (A) Cross-sectional area versus distance from nose tip comparison. (B) Hydraulic diameter versus distance from nose tip comparison.

narrower nasopharynx. The surface area and volume of each anatomical region generally increase with age. Notably, while the olfactory region has a larger surface area than the nasal vestibule and atrium, it has the smallest volume, highlighting its narrow, slit-like structure. The turbinate region has the largest surface area and volume among all partitions, with the most rapid growth during development, making it an essential component for maintaining the normal physiological function of the nasal cavity. Additionally, there are differences in the size of each anatomical partition of the left and right nasal cavity of the same individual, illustrating the asymmetric nature of the nasal cavity anatomy.

Fig. 7A compares the cross-sectional area of the nasal airway in children aged 3–12 years, with studies by Xi et al. [18] and Dong et al. [19] also included to validate the results. We found that the cross-sectional area of the nasal vestibule, starting from the nostril (approximately ~0–10 mm distance), is notably smaller. As the distance increases, the cross-sectional area of the turbinate region enlarges. For children aged 7–12 years, the cross-sectional area of the turbinate region grows rapidly, while for children aged 3–6 years, it increases slowly, maintaining around 200 mm. The cross-sectional area of the nasopharynx (distance ~> 55 mm) exhibits two trends of initial increase followed by decrease and a continuous decrease, which was mainly attributed to the anatomical abnormalities of the nasopharynx due to the occurrence of AH in some children. The trend of the nasal cavity cross-sectional area of the 5-year-old children's model in the present study was in good agreement with that of the reference model of the same age. Compared to adults, children have shorter lengths and smaller

cross-sectional areas in the nasal cavity and nasopharynx. Overall, the rapid growth of the nasal cavity at this age is shown in the characteristic of increasing cross-sectional area with age, except for two special cases at the ages of 7 and 12 years old, where a higher cross-sectional area occurs.

Fig. 7B compares the hydraulic diameter (H_D) of the nasal airway in children aged 3–12 years. The formula for the hydraulic diameter is $H_D = 4\,A/P$ (A: cross-sectional area, P: perimeter). For a circular tube the hydraulic diameter is simply the diameter of the tube. The results indicate that the hydraulic diameter of the nasal vestibule and nasal valve area in children is close to that of adults, approximately 5–7 mm. This indicates that as children grow from ages 3–12, the nasal vestibule region's overall shape becomes increasingly similar to that of adults. The presence of the superior, middle, and inferior turbinates makes the cross-sectional shape of the turbinate region more complex. The hydraulic diameter within this region decreases gradually, stabilizing at approximately 3–5 mm, in comparison to the larger nasal vestibule and nasal valve area. In the nasopharynx, however, the hydraulic diameter increases sharply, showing a fluctuating upward trend. Many studies [43–45] have shown that children at this age often suffer diseases such as AH, where local soft tissues thicken and protrude into the nasopharyngeal cavity, oropharynx adjacent to the retropalatal region, and hypopharynx (not included in the model), narrowing the local airway, and gradually atrophies after age of 10. This may be the main contributor to the undulation of the cross-sectional area and hydraulic diameter at the nasopharynx. Overall, the turbinate structure constitutes the main form
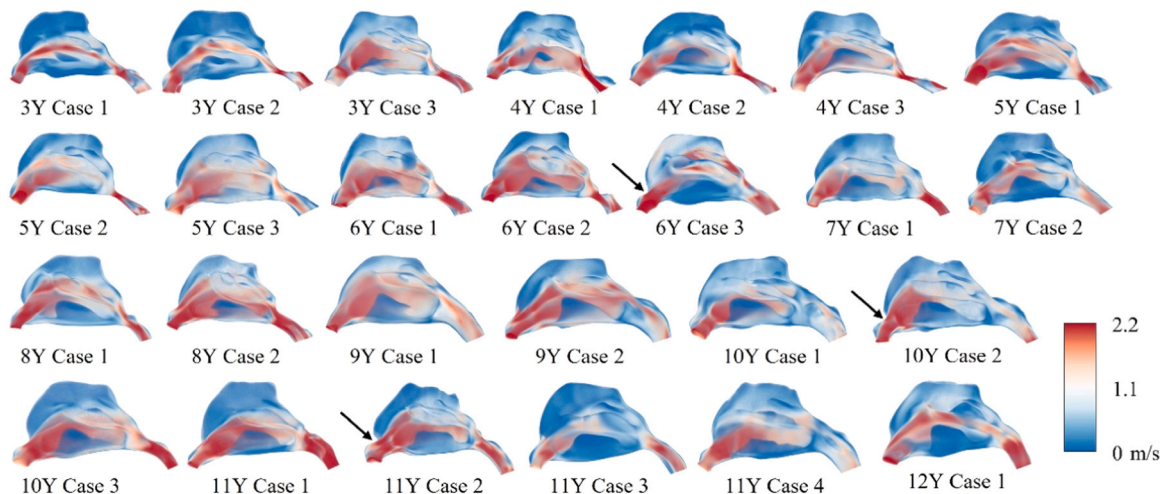

Fig. 8. Lateral perspective view of the velocity field. The black arrow points to the notch-like shape.
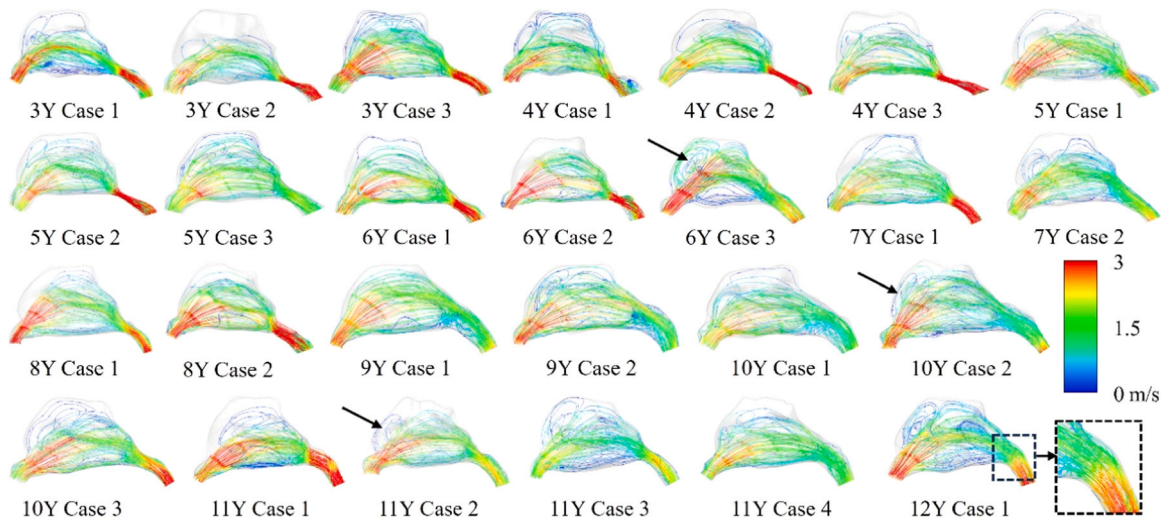
Fig. 9. Lateral view of the velocity streamlines. The black arrows indicate the airflow vortices, and the black boxes represent the nearly 90-degree bend formed by the airflow in the nasopharyngeal region.
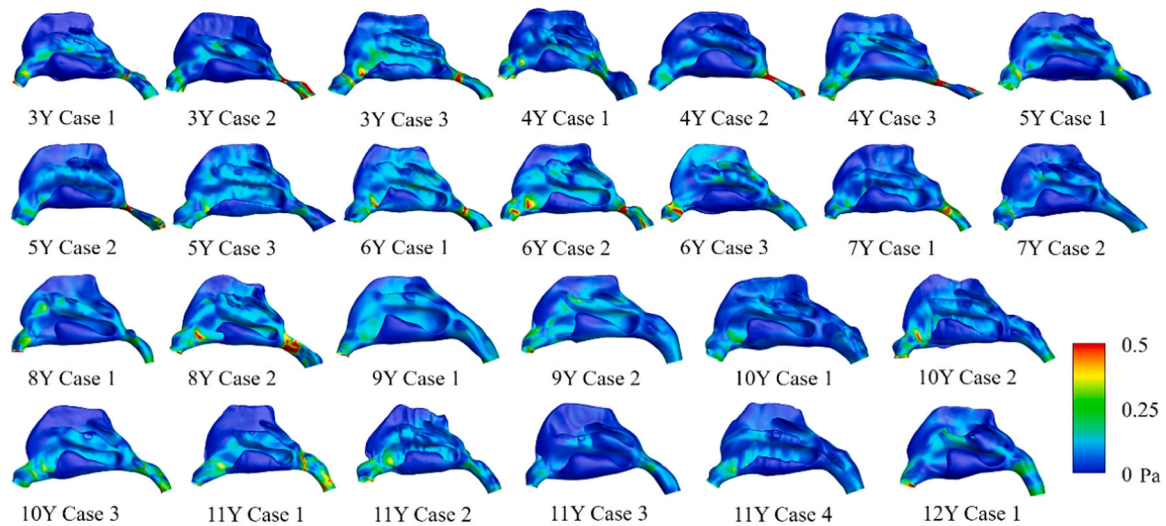

Fig. 10. Lateral view of the wall shear stress distributions.

of the complex shape of the nasal cavity. The trend of hydraulic diameter of 5-year-old children in this study is in general agreement with the findings of Dong et al. [19]. However, the hydraulic diameter of the anterior part of the nasal cavity, including the nasal vestibule (12.5–15 mm) and turbinate region (>8 mm), in the 5-year-old and 53-year-old models studied by Xi et al. [18], was significantly higher than that in the models in our study. Considering the comparison results of cross-sectional areas in Fig. 7A, the differences between subjects suggest that the cross-sectional perimeter of our study models is significantly larger than that of the models by Xi et al. [18], indicating that the nasal structure in the current study models is more complex. Overall, children's nasal cavities grow rapidly with age, gradually approaching adult size.

3.2. Airflow dynamics

As shown in Fig. 8 and Fig. 9, the airflow accelerates through the nasal vestibule and then into the narrower nasal valve. Most of the airflow travels through the middle and inferior meatus, while a smaller portion is directed upward into the olfactory region. The narrow, slit-like anatomical structures often induce turbulence in the olfactory

region. Unlike children, Dong et al.'s [19] study indicated that in 24-year-old adults, the majority of airflow was diverted to the widest nasal passage—the middle meatus, while in 77-year-old elderly individuals, inhalation airflow primarily passed through the inferior meatus, primarily due to the differences in their anatomical structures. Within the turbinate region of children, as the cross-sectional area increases, airflow velocity gradually decreases, and the streamlines become smoother, transitioning to laminar flow until reaching the nasopharynx. In some children, adenoid hypertrophy (AH) significantly narrows the nasopharyngeal airway, resulting in a marked increase in airflow velocity in this region. Upon entering the nasopharynx, airflow undergoes an abrupt 90-degree turn, forming noticeable vortices. The geometry of the nasal cavity, especially the shape of the vestibule, plays a substantial role in influencing the internal airflow field. According to the study by Inthavong et al. [46], the shape of the nasal vestibule can be classified into notched and non-notched types, and the airflow streamline through the non-notched type is less distorted and smoother, and the airflow is further diffused inside the nasal cavity. The nasal vestibules in 6-year-old case 3, 10-year-old case 2, and 11-year-old case 2 in this study exhibit a distinct notch-like shape, with significantly increased airflow velocity, and distinct airflow vortices were observed

Table 5
Flow partition (mean value) on the central cross-sectional plane slice in nasal cavity model.

3Y	Region ID	Volume flow rate (ml/s)	Flow partition	Region ID	Volume flow rate (ml/s)	Flow partition	Total partition (LC and RC)	% difference between RC and LC
	R1	1.09	0.83 %	L1	2.34	1.77 %	2.60 %	113.25 %
	R2	11.0	8.30 %	L2	11.5	8.68 %	16.98 %	4.58 %
	R3	28.6	21.72 %	L3	26.7	20.28 %	42 %	-6.63 %
	R4	2.31	1.75 %	L4	4.59	3.48 %	5.23 %	98.86 %
	R5	22.4	17.02 %	L5	20.6	15.63 %	32.65 %	-8.17 %
	R6	0.181	0.14 %	L6	0.481	0.36 %	0.50 %	157.14 %
	Total in RC		49.80 %	Total in LC		50.20 %		

4Y	Region ID	Volume flow rate (ml/s)	Flow partition	Region ID	Volume flow rate (ml/s)	Flow partition	Total partition (LC and RC)	% difference between RC and LC
	R1	4.46	3.08 %	L1	4.28	2.95 %	6.03 %	−4.22 %
	R2	8.26	5.70 %	L2	7.51	5.17 %	10.87 %	−9.30 %
	R3	36.2	24.95 %	L3	35.2	24.26 %	49.21 %	−2.77 %
	R4	8.67	5.98 %	L4	9.74	6.71 %	12.69 %	12.21 %
	R5	14.8	10.22 %	L5	14.9	10.26 %	20.48 %	0.39 %
	R6	0.411	0.28 %	L6	0.647	0.45 %	0.73 %	60.71 %
	Total in RC		50.20 %	Total in LC		49.80 %		

5Y	Region ID	Volume flow rate (ml/s)	Flow partition	Region ID	Volume flow rate (ml/s)	Flow partition	Total partition (LC and RC)	% difference between RC and LC
	R1	4.33	2.74 %	L1	4.73	3.00 %	5.74 %	9.49 %
	R2	16.5	10.47 %	L2	15.7	9.95 %	20.42 %	−4.97 %
	R3	30.9	19.56 %	L3	33.4	21.20 %	40.76 %	8.38 %
	R4	5.62	3.59 %	L4	5.62	3.56 %	7.15 %	−0.84 %
	R5	16.5	10.47 %	L5	22.5	14.27 %	24.74 %	36.29 %
	R6	0.959	0.61 %	L6	0.933	0.59 %	1.20 %	−3.28 %
	Total in RC		47.40 %	Total in LC		52.60 %		

6Y	Region ID	Volume flow rate (ml/s)	Flow partition	Region ID	Volume flow rate (ml/s)	Flow partition	Total partition (LC and RC)	% difference between RC and LC
	R1	7.94	4.56 %	L1	8.31	4.77 %	9.33 %	4.61 %
	R2	18.4	10.56 %	L2	19.7	11.32 %	21.88 %	7.20 %
	R3	27.6	15.85 %	L3	28.8	16.52 %	32.37 %	4.23 %
	R4	4.24	2.44 %	L4	8.64	4.96 %	7.40 %	103.28 %
	R5	22.7	13.03 %	L5	23.7	13.60 %	26.63 %	4.37 %
	R6	1.95	1.12 %	L6	2.20	1.26 %	2.38 %	12.50 %
	Total in RC		47.60 %	Total in LC		52.40 %		

7Y	Region ID	Volume flow rate (ml/s)	Flow partition	Region ID	Volume flow rate (ml/s)	Flow partition	Total partition (LC and RC)	% difference between RC and LC
	R1	2.75	1.50 %	L1	3.33	1.81 %	3.31 %	20.06 %
	R2	17.2	9.36 %	L2	13.5	7.37 %	16.73 %	−13.87 %
	R3	39.7	21.62 %	L3	45.2	24.63 %	46.25 %	13.73 %
	R4	2.68	1.44 %	L4	3.53	1.90 %	3.34 %	500.01 %
	R5	37.0	20.17 %	L5	17.6	9.59 %	29.76 %	−53.08 %
	R6	0.809	0.44 %	L6	0.299	0.16 %	0.61 %	−31.50 %
	Total in RC		54.50 %	Total in LC		45.50 %		

8Y	Region ID	Volume flow rate (ml/s)	Flow partition	Region ID	Volume flow rate (ml/s)	Flow partition	Total partition (LC and RC)	% difference between RC and LC
	R1	6.92	3.56 %	L1	5.76	2.96 %	6.53 %	−16.59 %
	R2	21.0	10.82 %	L2	21.6	11.10 %	21.92 %	2.58 %
	R3	30.8	15.85 %	L3	36.4	18.72 %	34.56 %	18.59 %
	R4	7.23	3.72 %	L4	5.53	2.85 %	6.57 %	−23.22 %
	R5	25.7	13.25 %	L5	32.5	16.74 %	29.99 %	29.01 %
	R6	0.479	0.25 %	L6	0.361	0.19 %	0.43 %	−12.29 %
	Total in RC		47.40 %	Total in LC		52.60 %		

9Y	Region ID	Volume flow rate (ml/s)	Flow partition	Region ID	Volume flow rate (ml/s)	Flow partition	Total partition (LC and RC)	% difference between RC and LC
	R1	5.16	2.54 %	L1	2.41	1.18 %	3.72 %	−5.80 %
	R2	24.0	11.78 %	L2	21.7	10.65 %	22.44 %	−9.51 %
	R3	44.6	21.91 %	L3	47.6	23.36 %	45.27 %	12.42 %
	R4	7.40	3.64 %	L4	6.90	3.39 %	7.03 %	−7.24 %
	R5	21.8	10.72 %	L5	19.8	9.74 %	20.47 %	−9.12 %
	R6	1.11	0.54 %	L6	1.08	0.53 %	1.08 %	22.02 %

Table 5 (*continued*)

	Total in RC		51.10 %	Total in LC		48.90 %		
10Y	Region ID	Volume flow rate (ml/s)	Flow partition	Region ID	Volume flow rate (ml/s)	Flow partition	Total partition (LC and RC)	% difference between RC and LC
	R1	4.47	2.38 %	L1	4.68	2.24 %	4.62 %	−24.15 %
	R2	20.0	10.14 %	L2	16.6	8.13 %	18.27 %	0.30 %
	R3	40.8	19.69 %	L3	45.6	22.08 %	41.77 %	14.74 %
	R4	10.5	5.06 %	L4	7.79	3.83 %	8.89 %	−19.40 %
	R5	28.8	13.96 %	L5	21.8	10.63 %	24.60 %	−17.28 %
	R6	1.68	0.89 %	L6	1.96	0.97 %	1.86 %	−18.55 %
	Total in RC		52.10 %	Total in LC		47.90 %		
11Y	Region ID	Volume flow rate (ml/s)	Flow partition	Region ID	Volume flow rate (ml/s)	Flow partition	Total partition (LC and RC)	% difference between RC and LC
	R1	0.608	0.50 %	L1	1.74	0.71 %	1.21 %	−179.72 %
	R2	30.7	14.12 %	L2	21.6	10.30 %	24.42 %	−27.11 %
	R3	51.6	23.40 %	L3	51.4	23.43 %	46.83 %	5.95 %
	R4	4.63	2.14 %	L4	2.88	1.42 %	3.56 %	−32.14 %
	R5	32.5	14.64 %	L5	18.5	8.61 %	23.25 %	−27.29 %
	R6	0.991	0.52 %	L6	0.448	0.21 %	0.73 %	−61.66 %
	Total in RC		55.30 %	Total in LC		44.70 %		
12Y	Region ID	Volume flow rate (ml/s)	Flow partition	Region ID	Volume flow rate (ml/s)	Flow partition	Total partition (LC and RC)	% difference between RC and LC
	R1	0.623	1.34 %	L1	1.10	2.38 %	3.72 %	76.91 %
	R2	2.10	4.53 %	L2	2.45	5.27 %	9.80 %	16.21 %
	R3	7.12	15.34 %	L3	6.85	14.76 %	30.10 %	−3.74 %
	R4	5.28	11.38 %	L4	6.95	14.97 %	26.35 %	31.46 %
	R5	6.17	13.28 %	L5	7.29	15.70 %	28.98 %	18.20 %
	R6	0.378	0.81 %	L6	0.109	0.24 %	1.05 %	−71.02 %
	Total in RC		46.70 %	Total in LC		53.30 %		

RC: right cavity, LC: left cavity.

behind them. The anatomical variability among pediatric subjects may further impact their intranasal drug delivery performance [47,48].

Combining Fig. 8 and Fig. 10 may be more helpful in understanding the influence of nasal airflow on nasal wall pressure. The overall wall shear stress generally ranges between 0 and 0.5 Pa, and generally high wall shear stress zone occurs in the same area as the high-velocity zone, namely the nasal valve region and the nasopharynx. Similarly, the wall shear stress in the nasal atrium, olfactory region, and inferior turbinate region is minimal, in correspondence with the minimal airflow velocities in these regions. Overall, the wall pressure decreases gradually from the anterior nostril to the nasopharynx. With increasing age, the nasal vestibule and nasal valve area in children continue to grow, gradually assuming a more elongated shape resembling that of adults. At the same time, the direction of the airflow in the vestibule region changes from going upward toward the vertical direction to the nostril to the cross-sectional plane in the main passage in the direction toward the nasopharynx, resulting in more significant shear stress being exerted on the wall as the airflow passes near the nasal valve. Due to the constriction of the nasopharyngeal airway leading to a significant increase in airflow velocity, the corresponding wall shear stress also notably higher.

3.3. Airflow partition

To enable a detailed analysis of the airflow within the nasal cavity, the central cross-sectional plane, positioned anterior to the superior turbinate, was divided into multiple regions based on the nasal meatus structure (Fig. 5B). We observe that most airflow passes through the main nasal passage and the middle meatus. Table 5 presents the airflow volume in each partition on the central cross-section of pediatric models aged 3–12 years, with the analysis based on average values within each age group.

In all age groups, a significantly greater amount of airflow is directed toward the lower part of the main nasal passage (R3/L3), the middle meatus (R5/L5), and the middle part of the main nasal passage (R2/L2). In contrast, airflow volume directed toward the olfactory region (R1/L1) and the inferior meatus (R4/L4) is very limited. In some cases, a negative value appears due to recirculating flow in this section. Given that children are still growing and their superior turbinates are not fully developed, its two characteristics reveal in this analysis: the tiny size of the superior turbinate and minimal airflow through the superior meatus (R6/L6 < 1.3 %).

For children aged 3–12 years, the airflow volume across different regions of the left and right nasal cavities varies, reflecting the asymmetrical anatomical structure of the nasal airway. Notably, the 11-year-old child exhibited the greatest difference in airflow volume between the two sides, with a disparity of 10.6 % (55.30 % vs. 44.70 %). Although there is a relatively high percentage difference between the left and right nasal cavities, the small absolute value of airflow volume means the overall impact on nasal airflow remains minimal.

3.4. Effect of virtual surgery on partitioned airflow

Table 6 presents the airflow volume across different partitions of the nasal cavity before and after virtual surgery. Following adenoidectomy, more airflow is diverted to the olfactory region, the middle of the main nasal passage, and the middle meatus, which aids in the olfactory perception in children. Conversely, there is a notable decrease in airflow volume through the lower part of the main nasal passage and the inferior meatus. For Subject 2 and Subject 5, the percentage difference in airflow volume between left and right nasal cavities reduced after virtual surgery, decreasing the airflow distribution imbalance and contributing to better realize the physiological function of the nasal cavity.

Fig. 11 depicts the comparison of airflow volume in each partition of the left and right nasal cavity before and after virtual surgery. As shown

Table 6
Airflow partition changes in subjects with adenoid hypertrophy before and after virtual surgery.

Subject 2	Region ID	Pre-operation		Post-operation	
		Flow partition	% difference between RC and LC	Flow partition	% difference between RC and LC
	R1 and L1	1.10 %	306.97 %	2.21 %	168.06 %
	R2 and L2	13.33 %	-10.52 %	15.18 %	-3.40 %
	R3 and L3	34.75 %	-6.29 %	33.16 %	9.22 %
	R4 and L4	3.33 %	208.24 %	1.15 %	59.13 %
	R5 and L5	47.19 %	-10.08 %	47.45 %	-9.09 %
	R6 and L6	0.31 %	353.99 %	0.86 %	25.16 %
Subject 5	Region ID	Pre-operation		Post-operation	
		Flow partition	% difference between RC and LC	Flow partition	% difference between RC and LC
	R1 and L1	1.68 %	−30.95 %	2.40 %	−27.87 %
	R2 and L2	16.04 %	−7.24 %	18.78 %	−2.09 %
	R3 and L3	55.09 %	40.77 %	52.34 %	29.59 %
	R4 and L4	9.15 %	52.94 %	6.53 %	0.24 %
	R5 and L5	17.78 %	18.06 %	19.46 %	11.84 %
	R6 and L6	0.28 %	−82.97 %	0.49 %	−34.88 %
Subject 6	Region ID	Pre-operation		Post-operation	
		Flow partition	% difference between RC and LC	Flow partition	% difference between RC and LC
	R1 and L1	5.47 %	19.86 %	6.51 %	21.12 %
	R2 and L2	9.25 %	−15.15 %	10.67 %	−19.15 %
	R3 and L3	43.34 %	−39.77 %	42.27 %	−35.78 %
	R4 and L4	20.48 %	−14.43 %	18.09 %	−22.17 %
	R5 and L5	20.14 %	−5.06 %	21.25 %	−7.52 %
	R6 and L6	1.32 %	14.75 %	1.21 %	41.00 %
Subject 8	Region ID	Pre-operation		Post-operation	
		Flow partition	% difference between RC and LC	Flow partition	% difference between RC and LC
	R1 and L1	9.87 %	−44.74 %	10.82 %	−32.37 %
	R2 and L2	19.88 %	−3.84 %	22.32 %	19.11 %
	R3 and L3	34.56 %	2.43 %	31.00 %	31.29 %
	R4 and L4	5.86 %	−41.48 %	5.01 %	−31.37 %
	R5 and L5	27.66 %	23.19 %	29.05 %	45.77 %
	R6 and L6	2.17 %	−3.94 %	1.80 %	26.50 %

in Fig. 11AB, the trends of airflow changes in each partition of the left and right nasal cavities before and after virtual surgery are generally similar, with airflow volume peaking at the lower part of the main passage (R3/L3) and the middle meatus (R5/L5). The airflow volume

directed towards the olfactory region (R1/L1) and the superior meatus (R6/L6) is notably less. Except for R5 in Subject 2 and L6 in Subject 6, airflow volumes in all other partitions show changes before and after virtual surgery, particularly with increased airflow volumes in the olfactory region. As shown in Fig. 11C, the absolute values of the differences in total airflow volume between the left and right nasal cavities before virtual surgery in the 4 children with AH were 1.8 % vs 11.6 % vs 13 % vs 1.6 %. After virtual surgery, the absolute values of the differences in total airflow volume between the left and right nasal cavities in the 4 children with AH were 0.4 % vs 7.2 % vs 12.6 % vs 8.8 % (Fig. 11D). With the exception of Subject 8, the difference in airflow volume between the left and right nasal cavities decreased after virtual surgery.

3.5. Effect of virtual surgery on nasal warming functions

As shown in Fig. 12AB, the peripheral temperature close to the nasal mucosa on the same cross-section was significantly higher than the temperature at the center. It is noteworthy that, regardless of original or virtual post-operative models, the temperature at the middle of each cross-section in the turbinate region (C5-C8) was significantly lower than that at the superior and inferior parts, with the temperature being highest at the superior part. This suggests that the middle part of the nasal cavity is the least effective at heating inhaled air, whereas the olfactory region provides the most effective heating.

Fig. 12C shows the trend of mean temperature changes across cross-sections was similar in both original and virtual post-operative models. Overall, the warming function was most prominent in the nasal valve region (C2, C3) and the turbinate region (C5-C8). The warming effect in the nasopharynx (C9-C11) was notably weaker, and the temperature of the airflow in this area tends to stabilize. This finding further enriches the previous research results [24,27,41]. For the original model, the initial temperature of the air inhaled through the nostrils was 293.00 K (20°C), which rapidly increased to 301.98 K at the nasal valve and further increased to 306.14 K at the choana. Compared to the original model, the mean temperature at each cross-section in the virtual post-operative model has decreased (except for cross-sections C0, C8, and C9). In the original model, the mean temperature increased in planes C12-C16 (the difference between the mean temperature of each plane and the temperature at the inlet) was more pronounced compared to the virtual post-operative model (13.51 ± 0.004 K vs 13.26 ± 0.003 K), with a significant difference ($P < 0.01$) (Fig. 14A), indicating a decrease in the warming capability of the virtual post-operative model. We believe this change occurs because, while adenoidectomy enlarges the volume of the nasopharynx, it simultaneously reduces the surface area of the nasal airway. This reduction limits the heat and moisture exchange between airflow and nasal mucosa. Therefore, this leads to a weakened warming and humidification function of the nasal cavity post-operatively. Temperature changes in the nasopharynx of the original and virtual post-operative models were not significantly correlated with airway surface area and volume, but were significantly correlated with airway surface area-to-volume ratio (SVR) (Table 7). Lindemann et al. [49] simulated intranasal airflow during inspiration after radical sinus surgery using CFD method and showed that aggressive sinus surgery resulted in disturbed air modulation in the nasal cavity. One point worthy of emphasis is the importance of protecting the nasal mucosa and avoiding excessive surgical intervention during various nasal cavity surgeries, thereby preventing the occurrence of post-operative complications associated with it.

3.6. Effect of virtual surgery on nasal humidification functions

Fig. 13AB show that the H_2O mass fraction near the nasal wall was significantly higher than that at the center within the same cross-section. This is primarily because peripheral airflow fully contacts the nasal mucosa, facilitating effective heat transfer and moisture exchange. In
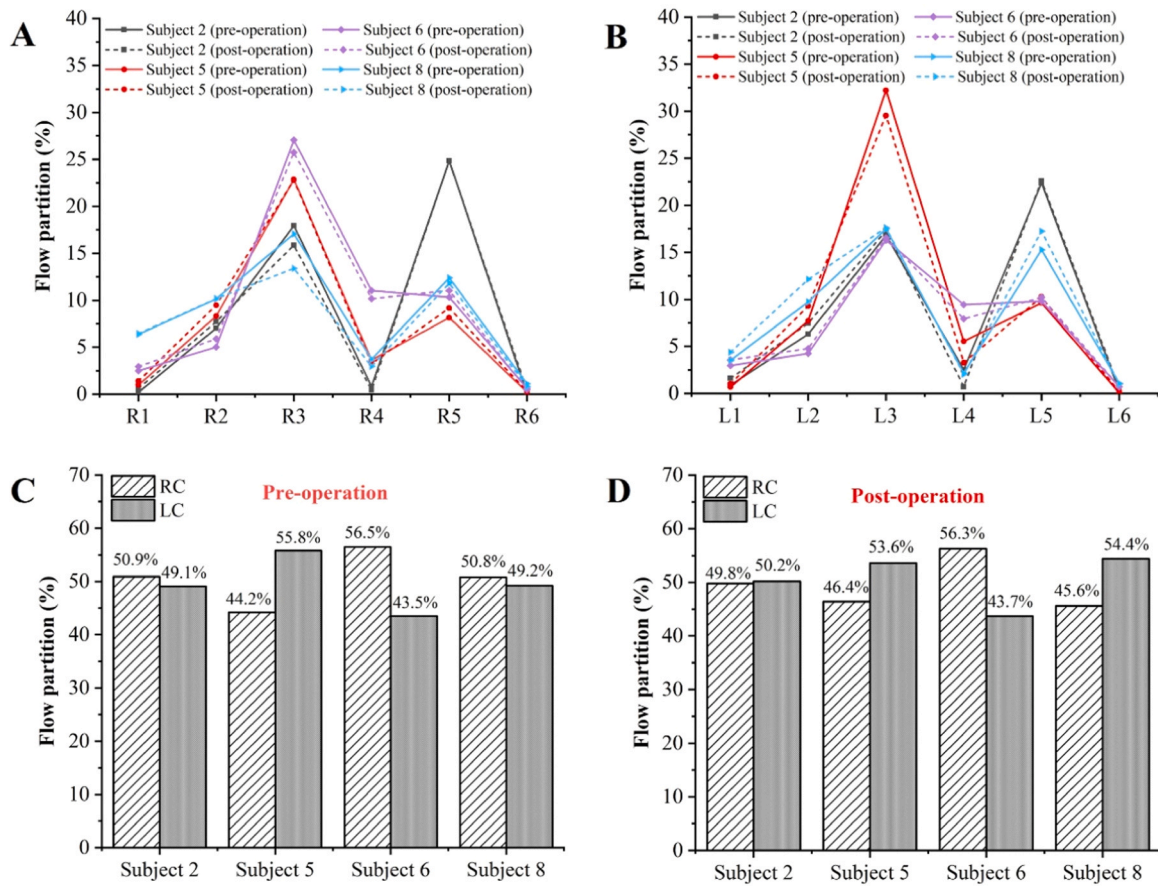
Fig. 11. Comparison of airflow volume in each partition of the right nasal cavity (A) and left nasal cavity (B) before and after virtual surgery. Comparison of airflow volume between the left and right nasal cavities before (C) and after (D) virtual surgery. RC: Right cavity, LC: Left cavity.
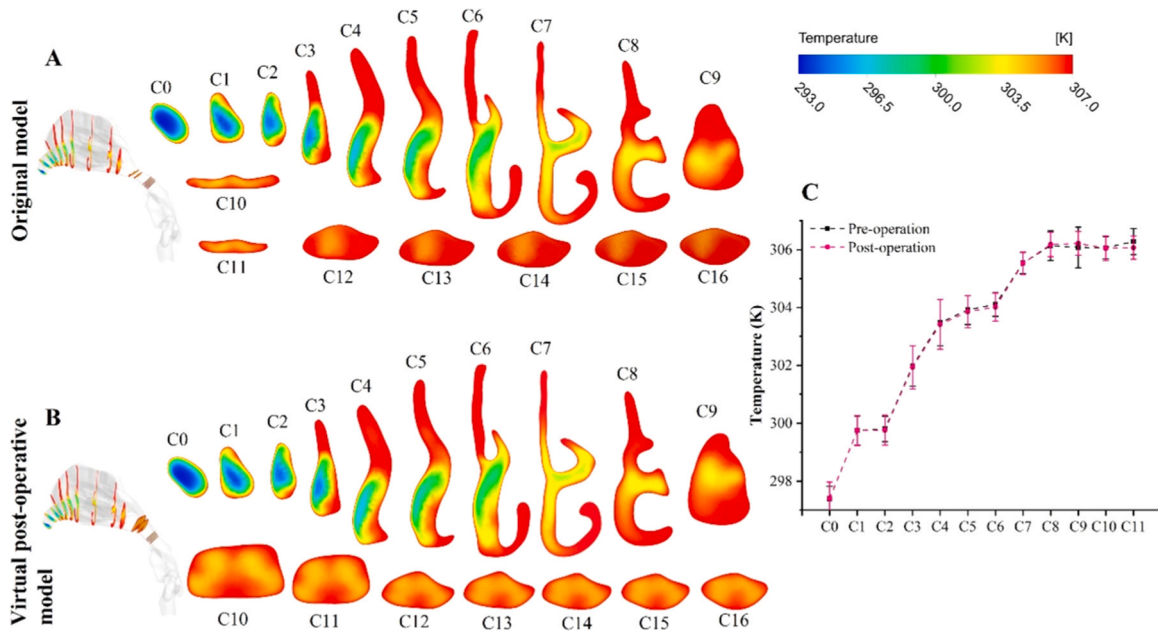

Fig. 12. Temperature contours on various cross-sections within the original (A) and virtual post-operative (B) models. (C) Trends in average temperature changes on various cross-sections within the models before and after virtual surgery.

both the original and virtual post-operative models, the turbinate region (C5-C8) displayed a notably lower H_2O mass fraction in the middle part compared to the superior and inferior parts, with the highest H_2O mass fraction found at the superior portion. This suggests that the middle part of the nasal cavity is the least effective at humidifying inhaled air, whereas the olfactory region provides the most effective humidification.
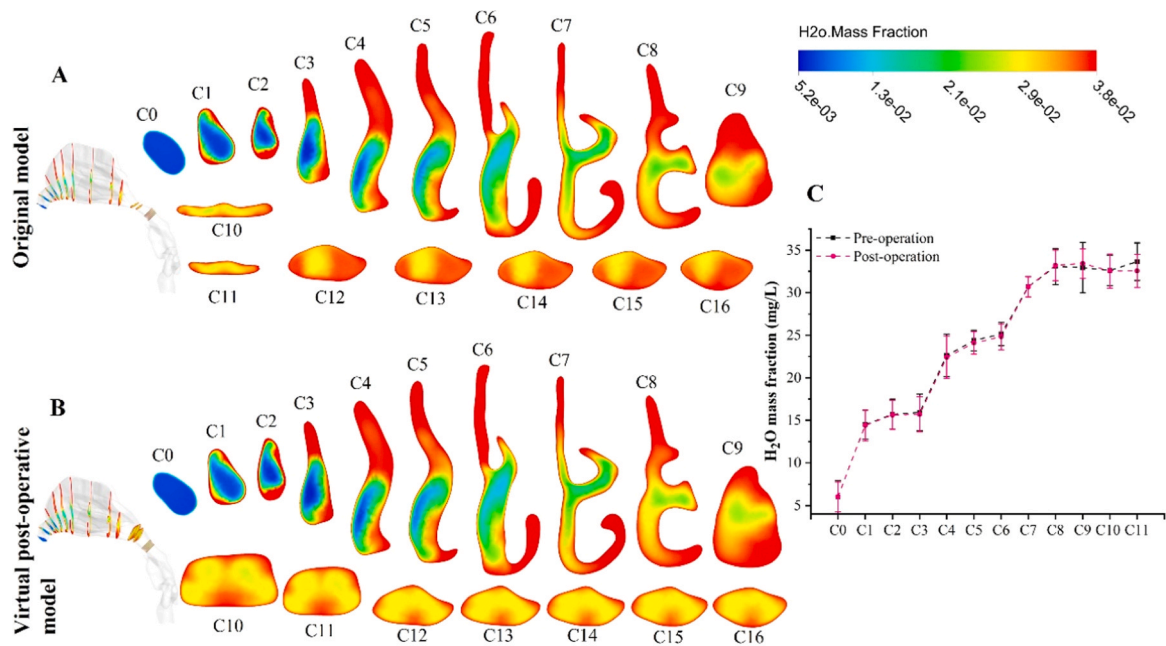
Fig. 13. H_2O mass fraction contours on various cross-sections within the original (A) and virtual post-operative (B) models. (C) Trends in average H_2O mass fraction changes on various cross-sections within the models before and after virtual surgery.
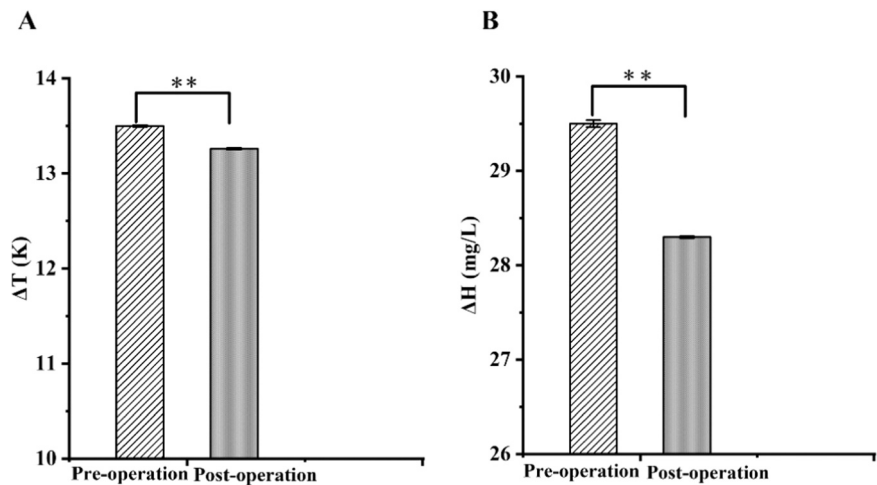

Fig. 14. Warming (A) and humidification (B) of the nasal cavity before and after virtual surgery, showing the mean differences at each pharyngeal cross-section (C12–16) and inlet (**: $P < 0.01$).

Table 7
Correlation between temperature of nasopharynx and area, volume and SVR of airway.

	Temperature of nasopharynx	
	Spearman r	P value
Area	0.072	0.866
Volume	−0.429	0.289
SVR	0.833	0.01

SVR: surface area-to-volume ratio.

This effect may be due to the olfactory region's large surface area and small volume, which enhances heat and moisture exchange between the air and nasal mucosa, thereby protecting the olfactory mucosa and nerves from irritation by dry, cold air.

As depicted in Fig. 13C, the trend of average H_2O mass fraction changes across cross-sections was similar between the original and virtual post-operative models. Humidification was most prominent in the nasal valve region (C2, C3) and the turbinate region (C5-C8), while it was noticeably weaker in the nasopharynx (C9-C11), where the H_2O mass fraction changes tended to stabilize. In the original model, the initial H_2O mass fraction of inhaled air was 5.18 mg/L, which increased rapidly to 15.93 mg/L at the nasal valve and further rose to 33.08 mg/L

Table 8
Correlation between H_2O mass fraction of nasopharynx and area, volume and SVR of airway.

	H_2O Mass Fraction of nasopharynx	
	Spearman r	P value
Area	0.18	0.67
Volume	−0.381	0.352
SVR	0.738	0.037

SVR: surface area-to-volume ratio.

at the choana. In the virtual post-operative model, the mean H_2O mass fraction at each cross-section generally decreased compared to the original model, except at cross-sections C0, C8, and C9. The original model showed a more pronounced mean H_2O mass fraction increase across planes C12-C16 (the difference between the mean humidity of each plane and the inlet humidity) than the virtual post-operative model (29.5 ± 0.037 mg/L vs. 28.3 ± 0.01 mg/L), with statistical significance ($P < 0.01$) (Fig. 14B). This indicates a reduction in humidification capacity in the virtual post-operative model. Changes in H_2O mass fraction between the pre- and post-surgery models were not significantly correlated with airway surface area or volume but showed a significant correlation with the surface area-to-volume ratio (SVR) (Table 8).

This study has some limitations. It only included steady-state calculations during the inhalation phase. To achieve more realistic conditions, a transient computational simulation of natural breathing should be considered and include both inhalation and exhalation phases. For the boundary treatment, the nasal wall is assumed to be smooth and rigid, without considering elasticity, displacement and deformation. Despite these limitations, the primary focus of this research is to analyze the effect of airway anatomical variation on airflow dynamics and nasal physiological function. Therefore, these assumptions are considered reasonable for the scope of this study. However, these assumptions will be further refined in future studies. In addition, the potential effects of gender and the cyclical nature of the nasal cycle on intranasal airflow characteristics will be further explored in subsequent research. While the current study is based on a RANS model, future work will consider more advanced simulation approaches such as Large Eddy Simulation (LES) or Direct Numerical Simulation (DNS), which offer improved resolution of transient and turbulent flow structures, and thus may provide deeper insights into the complex airflow dynamics within the nasal cavity.

4. Conclusion

This study systematically analyzed the geometric characteristics, aerodynamic performance and partitioned airflow volume of the nasal cavities in Asian children subjects aged 3–12 years, and explores the nasal warming and humidification functions before and after virtual surgery. Anatomically, the nasal cavity in this age group shows rapid growth, with an overall trend of increasing size with age, gradually approaching adult geometry. Growth in the turbinate area is particularly notable and constitutes the main form of the complex shape of the nasal cavity. Similar to adults, children's nasal vestibule shapes vary and can be categorized as notched or non-notched types, which significantly impact airflow patterns and vortex formation within the cavity. Local airflow analysis showed that the airflow in children's nasal cavities concentrated at the junction of the main nasal passage and the middle meatus, with a difference in airflow volume between the left and right sides. Post-virtual adenoidectomy, more airflow is redirected to the olfactory area, the middle of the main nasal passage, and the middle meatus, which helps to reduce the imbalance in airflow distribution between the left and right nasal cavities. However, the warming and humidification function of the nasal cavity was diminished post-surgery, especially in the nasopharynx, and this reduction correlated primarily with the airway's surface area-to-volume ratio (SVR). These findings contribute to a deeper understanding of the nasal anatomy and airflow dynamics in the pediatric population, and support the development of patient-centered surgical plans for optimal outcomes. Furthermore, the results may be applicable to other ethnic groups if inter-ethnic similarities can be demonstrated.

This study reveals the substantial impact of adenoid hypertrophy on nasal airflow characteristics and airflow regulation function. In clinical practice, beyond assessing the degree of nasopharyngeal narrowing on CT images, numerical simulation data, such as olfactory cleft ventilation volume and the warming and humidifying capacity of the nasopharynx, can also be incorporated to comprehensively evaluate surgical indications and develop more scientifically informed intervention strategies. Furthermore, virtual adenoidectomy using CFD allows for the prediction of postoperative improvements in nasal ventilation and physiological function, showing great promise for integration into precision diagnosis and individualized treatment planning for otolaryngologic disorders. In future clinical practice, by further expanding the database of pediatric nasal airway models and developing a virtual surgical simulation platform, multicenter collaborative studies can be promoted to incorporate personalized pediatric airway modeling and simulation into routine clinical assessment, diagnostic support, and surgical planning, thereby advancing the digital, visualized, and individualized management of the pediatric upper airway.

CRediT authorship contribution statement

Zhenzhen Hu: Conceptualization, Data curation, Methodology, Formal analysis, Software, Validation, Writing – original draft. **Junming Chen:** Methodology, Data curation, Writing – original draft. **Ya Zhang:** Funding acquisition, Conceptualization, Methodology, Formal analysis, Writing – review & editing. **Ying Wang:** Conceptualization, Validation, Methodology. **Yulin Zhao:** Software, Validation, Investigation. **Guoxi Zheng:** Formal analysis, Visualization. **Shaokoon Cheng:** Methodology, Writing – review & editing. **Kiao Inthavong:** Methodology, Writing – review & editing. **Jingliang Dong:** Project administration, Supervision, Funding acquisition, Conceptualization, Methodology, Formal analysis, Writing – review & editing.

Declaration of Competing Interest

All authors declare that we have no known competing financial interests or personal relationships that could have appeared to influence the work reported in this paper.

Acknowledgements

Data availability

Data will be made available on request.

References

[1] G.K. Reznik, Comparative anatomy, physiology, and function of the upper respiratory tract, Environ. Health Perspect. 85 (1990) 171–176, https://doi.org/10.1289/ehp.85-1568330.

[2] D. Han, L. Zhang, Clinical evaluation of nasal physiology, J. Cap. Med. Univers. 30 (2009) 44–48.

[3] L. Lambert, F.J. Culley, Innate immunity to respiratory infection in early life, Front. Immunol. 8 (2017) 1570, https://doi.org/10.3389/fimmu.2017.01570.

[4] P. Cole, Further observations on the conditioning of respiratory air, J. Laryngol. Otol. 67 (1953) 669–681, https://doi.org/10.1017/s0022215100049161.

[5] J. Boyce, R. Eccles, Do chronic changes in nasal airflow have any physiological or pathological effect on the nose and paranasal sinuses? A systematic review, Clin. Otolaryngol. 31 (2006) 15–19, https://doi.org/10.1111/j.1749-4486.2006.01125.x.

[6] J.S. Kimbell, D.O. Frank, P. Laud, G.J. Garcia, J.S. Rhee, Changes in nasal airflow and heat transfer correlate with symptom improvement after surgery for nasal obstruction, J. Biomech. 46 (2013) 2634–2643, https://doi.org/10.1016/j.jbiomech.2013.08.007.

[7] S. Ozlugedik, G. Nakiboglu, C. Sert, A. Elhan, E. Tonuk, S. Akyar, I. Tekdemir, Numerical study of the aerodynamic effects of septoplasty and partial lateral turbinectomy, Laryngoscope 118 (2008) 330–334, https://doi.org/10.1097/MLG.0b013e318159aa26.

[8] G.J. Garcia, J.S. Rhee, B.A. Senior, J.S. Kimbell, Septal deviation and nasal resistance: an investigation using virtual surgery and computational fluid dynamics, Am. J. Rhinol. Allergy 24 (2010) e46–e53, https://doi.org/10.2500/ajra.2010.24.3428.

[9] S. Alam, C. Li, K.H. Bradburn, K. Zhao, T.S. Lee, Impact of middle turbinectomy on airflow to the olfactory cleft: a computational fluid dynamics study, Am. J. Rhinol. Allergy 33 (2019) 263–268, https://doi.org/10.1177/1945892418816841.

[10] L. Pereira, J. Monyror, F.T. Almeida, F.R. Almeida, E. Guerra, C. Flores-Mir, C. Pacheco-Pereira, Prevalence of adenoid hypertrophy: a systematic review and meta-analysis, Sleep. Med. Rev. 38 (2018) 101–112, https://doi.org/10.1016/j.smrv.2017.06.001.

[11] G.C. Goeringer, B. Vidic, The embryogenesis and anatomy of Waldeyer's ring, Otolaryngol. Clin. North. Am. 20 (1987) 207–217.

[12] C.L. Marcus, L.J. Brooks, K.A. Draper, D. Gozal, A.C. Halbower, J. Jones, M. S. Schechter, S.H. Sheldon, K. Spruyt, S.D. Ward, C. Lehmann, R.N. Shiffman, Diagnosis and management of childhood obstructive sleep apnea syndrome, Pediatrics 130 (2012) 576–584, https://doi.org/10.1542/peds.2012-1671.

[13] B.S. Turkoglu, E. Aydin, Adenoidectomy: current approaches and review of the literature, Kulak Burun Bogaz Ihtis. Derg. 26 (2016) 181–190, https://doi.org/10.5606/kbbihtisas.2016.32815.

[14] R. Hebbink, B.J. Wessels, R. Hagmeijer, K. Jain, Computational analysis of human upper airway aerodynamics, Med. Biol. Eng. Comput. 61 (2023) 541–553, https://doi.org/10.1007/s11517-022-02716-8.

[15] P. Nithiarasu, O. Hassan, K. Morgan, N.P. Weatherill, C. Fielder, H. Whittet, P. Ebden, K.R. Lewis, Steady flow through a realistic human upper airway geometry, Int. J. Numer. Meth. Fluids 57 (2008) 631–651, https://doi.org/10.1002/fld.1805.

[16] T.B. Martonen, L. Quan, Z. Zhang, C.J. Musante, Flow simulation in the human upper respiratory tract, Cell Biochem. Biophys. 37 (2002) 27–36, https://doi.org/10.1385/CBB:37:1:27.

[17] J. Xi, X. Si, J.W. Kim, A. Berlinski, Simulation of airflow and aerosol deposition in the nasal cavity of a 5-year-old child, J. Aerosol Sci. 42 (2011) 156–173, https://doi.org/10.1016/j.jaerosci.2010.12.004.

[18] J. Xi, X. Si, Y. Zhou, J. Kim, A. Berlinski, Growth of nasal and laryngeal airways in children: implications in breathing and inhaled aerosol dynamics, Respir. Care 59 (2014) 263–273, https://doi.org/10.4187/respcare.02568.

[19] J. Dong, Q. Sun, Y. Shang, Y. Zhang, L. Tian, J. Tu, Numerical comparison of inspiratory airflow patterns in human nasal cavities with distinct age differences, Int. J. Numer. Method Biomed. Eng. 38 (2022) e3565, https://doi.org/10.1002/cnm.3565.

[20] Q. Sun, Y. Zhang, L. Tian, J. Tu, R. Corley, A.P. Kuprat, J. Dong, Investigation of inter-subject variation in ultrafine particle deposition across human nasal airways: a study involving children, adults, and the elderly, Sci. Total Environ. 955 (2024) 177028, https://doi.org/10.1016/j.scitotenv.2024.177028.

[21] Y. Zhou, M. Guo, J. Xi, H. Irshad, Y.S. Cheng, Nasal deposition in infants and children, J. Aerosol Med. Pulm. Drug Deliv. 27 (2014) 110–116, https://doi.org/10.1089/jamp.2013.1039.

[22] B.K. Samolinski, A. Grzanka, T. Gotlib, Changes in nasal cavity dimensions in children and adults by gender and age, Laryngoscope 117 (2007) 1429–1433, https://doi.org/10.1097/MLG.0b013e318064e837.

[23] Z. Hu, J. Dong, M. Lou, J. Zhang, R. Ma, Y. Wang, M. Gong, B. Wang, Z. Tong, H. Ren, G. Zheng, Y. Zhang, Effect of different degrees of adenoid hypertrophy on pediatric upper airway aerodynamics: a computational fluid dynamics study, Biomech. Model Mechanobiol. 22 (2023) 1163–1175, https://doi.org/10.1007/s10237-023-01707-4.

[24] E. Moreddu, L. Meister, A. Dabadie, J.M. Triglia, M. Medale, R. Nicollas, Numerical simulation of nasal airflows and thermal air modification in newborns, Med. Biol. Eng. Comput. 58 (2020) 307–317, https://doi.org/10.1007/s11517-019-02092-w.

[25] T. Keck, R. Leiacker, A. Heinrich, S. Kuhnemann, G. Rettinger, Humidity and temperature profile in the nasal cavity, Rhinology 38 (2000) 167–171.

[26] T. Keck, R. Leiacker, H. Riechelmann, G. Rettinger, Temperature profile in the nasal cavity, Laryngoscope 110 (2000) 651–654, https://doi.org/10.1097/00005537-200004000-00021.

[27] F. Sommer, R. Kroger, J. Lindemann, Numerical simulation of humidification and heating during inspiration within an adult nose, Rhinology 50 (2012) 157–164, https://doi.org/10.4193/Rhino11.231.

[28] S. Hanida, F. Mori, K. Kumahata, M. Watanabe, S. Ishikawa, T. Matsuzawa, Influence of latent heat in the nasal cavity, J. Biomech. Sci. Eng. 8 (2013) 209–224, https://doi.org/10.1299/jbse.8.209.

[29] K. Wiesmiller, T. Keck, R. Leiacker, J. Lindemann, Simultaneous in vivo measurements of intranasal air and mucosal temperature, Eur. Arch. Otorhinolaryngol. 264 (2007) 615–619, https://doi.org/10.1007/s00405-006-0232-6.

[30] A. Dayal, J.S. Rhee, G.J. Garcia, Impact of middle versus inferior total turbinectomy on nasal aerodynamics, Otolaryngol. Head Neck Surg. 155 (2016) 518–525, https://doi.org/10.1177/0194599816644915.

[31] D. Hsu, M. Chuang, In-vivo measurements of micrometer-sized particle deposition in the nasal cavities of taiwanese adults, Aerosol Sci. Tech. 46 (2012) 631–638, https://doi.org/10.1080/02786826.2011.652749.

[32] M.T. Laine-Alava, S. Murtolahti, U.K. Crouse, D.W. Warren, Guideline values for minimum nasal cross-sectional area in children, Cleft Palate Craniofac. J. 55 (2018) 1043–1050, https://doi.org/10.1177/1055665618767107.

[33] M. Fujioka, L.W. Young, B.R. Girdany, Radiographic evaluation of adenoidal size in children: adenoidal-nasopharyngeal ratio, AJR Am. J. Roentgenol. 133 (1979) 401–404, https://doi.org/10.2214/ajr.133.3.401.

[34] S. Elwany, The adenoidal-nasopharyngeal ratio (AN ratio). Its validity in selecting children for adenoidectomy, J. Laryngol. Otol. 101 (1987) 569–573, https://doi.org/10.1017/s0022215100102269.

[35] T.O. Adedeji, Y.B. Amusa, A.A. Aremu, Correlation between adenoidal nasopharyngeal ratio and symptoms of enlarged adenoids in children with adenoidal hypertrophy, Afr. J. Paediatr. Surg. 13 (2016) 14–19, https://doi.org/10.4103/0189-6725.181701.

[36] Z. Hu, R. Ma, Y. Wang, M. Lou, M. Gong, B. Wang, G. Zheng, J. Dong, Y. Zhang, Quantitative study of Artemisia pollens deposition in the upper airways of children with adenoidal hypertrophy, J. Aerosol Sci. 172 (2023) 106191, https://doi.org/10.1016/j.jaerosci.2023.106191.

[37] M. Spiegel, T. Redel, Y.J. Zhang, T. Struffert, J. Hornegger, R.G. Grossman, A. Doerfler, C. Karmonik, Tetrahedral vs. polyhedral mesh size evaluation on flow velocity and wall shear stress for cerebral hemodynamic simulation, Comput. Methods Biomech. Biomed. Eng. 14 (2011) 9–22, https://doi.org/10.1080/10255842.2010.518565.

[38] J. Wen, K. Inthavong, J. Tu, S. Wang, Numerical simulations for detailed airflow dynamics in a human nasal cavity, Respir. Physiol. Neurobiol. 161 (2008) 125–135, https://doi.org/10.1016/j.resp.2008.01.012.

[39] Y. Shang, J. Dong, F. He, K. Inthavong, L. Tian, J. Tu, Detailed comparative analysis of environmental microparticle deposition characteristics between human and monkey nasal cavities using a surface mapping technique, Sci. Total Environ. 853 (2022) 158770, https://doi.org/10.1016/j.scitotenv.2022.158770.

[40] W. Hofmann, Mathematical model for the postnatal growth of the human lung, Respir. Physiol. 49 (1982) 115–129, https://doi.org/10.1016/0034-5687(82)90106-2.

[41] J. Lindemann, T. Keck, K. Wiesmiller, B. Sander, H.J. Brambs, G. Rettinger, D. Pless, A numerical simulation of intranasal air temperature during inspiration, Laryngoscope 114 (2004) 1037–1041, https://doi.org/10.1097/00005537-200406000-00015.

[42] L. Tian, J. Dong, Y. Shang, J. Tu, Detailed comparison of anatomy and airflow dynamics in human and cynomolgus monkey nasal cavity, Comput. Biol. Med. 141 (2022) 105150, https://doi.org/10.1016/j.compbiomed.2021.105150.

[43] D.Y. Wang, N. Bernheim, L. Kaufman, P. Clement, Assessment of adenoid size in children by fibreoptic examination, Clin. Otolaryngol. Allied Sci. 22 (1997) 172–177, https://doi.org/10.1046/j.1365-2273.1997.00002.x.

[44] R. Arens, C.L. Marcus, Pathophysiology of upper airway obstruction: a developmental perspective, Sleep 27 (2004) 997–1019, https://doi.org/10.1093/sleep/27.5.997.

[45] M.A. Khan, F.U.H. Nawaz, A. Hakim, M. Khan, Frequency of adenoid hypertrophy among adult patients with nasal obstruction, J. Postgrad. Med. Inst. 32 (2018) 262–265.

[46] K. Inthavong, J. Ma, Y. Shang, J. Dong, A. Chetty, J. Tu, D. Frank-Ito, Geometry and airflow dynamics analysis in the nasal cavity during inhalation, Clin. Biomech. (Bristol Avon). 66 (2019) 97–106, https://doi.org/10.1016/j.clinbiomech.2017.10.006.

[47] M. Hejazi, A.M. Alshammary, D.J. Edwards, L. Golshahi, Development of a predictive model for pediatric intranasal drug delivery with nasal sprays: Leveraging intersubject variability in anatomical dimensions, administration-related parameters, and airway patency, Comput. Biol. Med. 187 (2025) 109746, https://doi.org/10.1016/j.compbiomed.2025.109746.

[48] A.R. Esmaeili, J.V. Wilkins, S. Hosseini, A. Alfaifi, M. Hejazi, M. Hindle, W. Longest, T. Schuman, S. Dhapare, A. Kaviratna, R. Walenga, B. Newman, L. Golshahi, In vitro evaluation of intersubject variability in pediatric intranasal drug delivery using nasal spray suspension products, J. Aerosol Sci. 179 (2024) 106387, https://doi.org/10.1016/j.compbiomed.2025.109746.

[49] J. Lindemann, H.J. Brambs, T. Keck, K.M. Wiesmiller, G. Rettinger, D. Pless, Numerical simulation of intranasal airflow after radical sinus surgery, Am. J. Otolaryngol. 26 (2005) 175–180, https://doi.org/10.1016/j.amjoto.2005.02.010.